

H₂O Masers and Protoplanetary Disk Dynamics in IC 1396 N

O. S. Bayandina^{1*}, I. E. Val'tts¹, S. E. Kurtz², G. M. Rudnitskij³, and A. V. Alakoz¹

¹*Astro Space Center, Lebedev Physical Institute, Russian Academy of Sciences, Moscow, 117997 Russia*

²*Instituto de Radioastronomía y Astrofísica, Universidad Nacional Autónoma de México, Morelia, México*

³*Moscow State University, Sternberg Astronomical Institute, Moscow, Russia*

Abstract—We report H₂O maser line observations of the bright-rimmed globule IC 1396 N using a ground-space interferometer with the 10-m RadioAstron radio telescope as the space-based element. The source was not detected on projected baselines >2.3 Earth diameters, which indicates a lower limit on the maser size of $L > 0.03$ AU and an upper limit on the brightness temperature of 6.25×10^{12} K. Fringe-rate maps are prepared based on data from ground-ground baselines. Positions, velocities and flux densities of maser spots were determined. Multiple low-velocity features from -4.5 km/s to $+0.7$ km/s are seen, and two high-velocity features of $V_{\text{LSR}} = -9.4$ km/s and $V_{\text{LSR}} = +4.4$ km/s are found at projected distances of 157 AU and 70 AU, respectively, from the strongest low-velocity feature at $V_{\text{LSR}} = \sim +0.3$ km/s. Maser components from the central part of the spectrum fall into four velocity groups but into three spatial groups. Three spatial groups of low-velocity features detected in the 2014 observations are arranged in a linear structure about ~ 200 AU in length. Two of these groups were not detected in 1996 and possibly are jets which formed between 1996 and 2014. The putative jet seems to have changed direction in 18 years, which we explain by the precession of the jet under the influence of the gravity of material surrounding the globule. The jet collimation can be provided by a circumstellar protoplanetary disk. There is a straight line orientation in the “ V_{LSR} -Right Ascension” diagram between the jet and the maser group at $V_{\text{LSR}} = \sim +0.3$ km/s. However, the central group with the same position but at the velocity $V_{\text{LSR}} \sim -3.4$ km/s falls on a straight line between two high-velocity components detected in 2014. Comparison of the low-velocity positions from 2014 and 1996, based on the same V_{LSR} -Right Ascension diagram for low-velocity features, shows that the majority of the masers maintain their positions near the central velocity $V_{\text{LSR}} = \sim 0.3$ km/s during the 18 year period.

DOI: 10.1134/S1063772917060026

1. INTRODUCTION

1.2. Masers

1.1. General Information

IC 1396 N is a cometary, bright-rimmed globule in the northern part of the HII region IC 1396 located at a distance of 750 pc [1]. There is the brightest source among the 25 IRAS point sources embedded in the nebula, with a far infrared luminosity of $440 L_{\odot}$ [2]. It is the intermediate-mass protostar IRAS 21391+5802. Multiple young stellar objects (YSO) at different evolutionary stages are located in the globule, and have been detected by their millimeter continuum emission [3, 4]. The BIMA-2 molecular core, the most prominent source at 3.1 mm, is the center of several bipolar molecular flows observed in wings of many thermal lines (see [2, 3, 5, 6] and references therein).

H₂O maser emission in the region was first reported by [7]. Although IC 1396 N/BIMA-2 has been searched for OH emission various times, no such masers have been found. OH emission in IC 1396 N was not found with the Nançay radio telescope (France) in 2002–2003 [8]. We also observed IC 1396 N in the OH lines at frequencies 1665 and 1667 MHz at the velocity range $V_{\text{LSR}} = -35 \dots +35$ km/s with the Nançay radio telescope in 2007 with null results at a 3σ level of 0.1 Jy. Methanol class II maser emission at 6.7 GHz [9], commonly found in accretion disks, is not present, but there is Class I methanol maser emission at 44 GHz [10], which indicates a very early stage of the compression of protostellar matter. No information is available about possible association with Infrared Dark Clouds [11] or Spitzer Dark Clouds [12] (IRDC/SDC) or with Extended Green Objects (EGO) [13].

*E-mail: bayandina@asc.rssi.ru

1.3. VLA and VLBA Studies

In 1992 IC 1396 N was mapped in the H₂O maser line using the VLA with an angular resolution of 0.1'' [14]: they found a group of three maser spots within 0.18'' (135 AU) of one another and a separate component at a distance of 13.3'' (10⁴ AU). Their monitoring program showed that the H₂O masers in IC 1396 N are variable in both velocity and flux density.

In June 1996 the H₂O masers in IC 1396 N were observed with the VLBA as part of the prelaunch VSOP survey; the angular resolution was of order 0.3 mas [15]. A more complete analysis of the VSOP survey data was presented by [16]. Their image, made with a 1.0 × 0.3 mas restoring beam, shows an aligned chain of maser spots about 15 AU in extent. The strongest maser component, at $V_{\text{LSR}} = +0.5$ km/s, was unresolved on the shortest baseline, with a correlated flux density of about 150 Jy. This was the strongest H₂O maser flux density ever observed from IC 1396 N since its discovery in 1988 [7]. The VLBA observations also revealed two high-velocity features at −14.1 km/s and at +9.3 km/s were observed at distances of 410 AU and 10 000 AU from the center of the cluster, respectively.

Three models were proposed by [16]: (i) a Keplerian disk, (ii) a stellar wind, and (iii) a molecular outflow. A combination of these models was also discussed by [16]. They suggest that the low-velocity features arise in the Keplerian disk with maser emission excited by shock waves, while the high-velocity features arise at the root of the molecular outflow originating from the central 4 M_{\odot} young star or protostar. The mass of the disk and its angular momentum are similar to those of the Solar System. It is suggested that it is a circumstellar accretion disk accumulating the excess angular momentum of the collapsing molecular core, which may give rise to the formation of a protoplanetary system.

In [17] the H₂O masers were observed with both single-dish telescopes and interferometers. Their VLBA observations had a synthesized beam of 0.8 × 0.4 mas (0.6 × 0.3 AU). These observations were made in 1996 in three epochs—March, April, and May, with 1 month interval. I.e. just before the observations of [15, 16], but the paper [17] was published later than [16]. The authors found a loop of maser spots within 1 AU and a few higher velocity components moving away from the loop; the average proper motion of the masers was 2 mas per year. They interpreted this picture as a bipolar outflow rather than a large-scale disk, though the disk model could be valid for the features closest to the central star. It was concluded that additional observations may still reveal some rotation or even “infall” toward the

source. In [17] a strong variability of the maser in 1995–1996 was also observed.

Of particular interest is the model proposed in [18–20], in which “curved” and “twisted” filaments of H₂O masers can be found, formed as a result of the circumstellar protoplanetary disk precession. This model assumes that a small gas-dust disk is surrounded by a massive near-star torus, which remains from the protostar clusters and from which a new star is forming. The axis of the disk is inclined at some angle to the torus, making the disc precess. The outflow is collimated by the disc and carries away material from the internal walls of the torus, exciting masers where the material strikes the torus walls. A large-scale bipolar flow is directed through the polar regions of the torus. An example of this model is the spiral nebula NGC 2261 (the Hubble Nebula)[21].

Using the model of the precessing disk, along with the estimated size and mass of the system, it can be shown that the precession period is of the order of decades. Under the influence of the shock wave, maser spots’ proper motion can reach 1–2 mas per year and may be traced over short time intervals in observations with a resolution of (0.1–0.01) mas.

The relatively close distance of this source as well as the presence of several YSOs, outflows, and possibly a protoplanetary disk or protostellar wind, make it an ideal laboratory for the study of the general aspects of the process of star formation.

We have monitored the H₂O masers in IC 1396 N with the RT-22 radio telescope in Pushchino (Moscow region) for more than twenty years. Although these observations cannot resolve the masers’ spatial structure, they do provide a long history of the spectral behavior. Our observations show that the peak flux density can reach values of 100 Jy, while the spectral features appear and disappear at different radial velocities. These fluctuations mean that any study of the maser spots’ proper motions should be done on relatively short timescales to ensure the unique identification of each maser spot being followed.

Positions of maser spots in multiple epochs can be obtained to a high accuracy from VLBI observations with baselines larger than the diameter of the Earth. With this goal, an experiment has been made using the spaceborne RadioAstron telescope and a network of ground-based radio telescopes. The results are reported in this paper. In these observations proper motions can be detected on timescales of a few months, allowing us to determine the spatial structure of the masers and to trace the dynamics of the maser spots for comparison with the models discussed in [16, 17]. Furthermore, observations with high spatial resolution using RadioAstron can provide information

Table 1. Baseline length and effective resolution implemented in the observations at the ground-space baselines

Session number	Month	Average projected baseline, ED	Average projected baseline, km	Average projected baseline, $10^9\lambda$	Effective resolution, 10^{-9} radian	Effective resolution, mas
1	July	2.3	29310	2.2	0.46	95
2	October	3.8	48420	3.6	0.28	58
3	November	5.9	75178	5.6	0.18	37
4	December	5.1	64984	4.8	0.21	43
5	December	3.8	48420	3.6	0.28	58

Table 2. List of radio telescopes participating in H₂O maser observations of IC 1396 N in 2014

Session number	Date	Session duration, hours	Radio telescopes*	Session beginning	Session end	Flux density,** Jy
1	2014-07-26	3	Ys, Nt, Sr, Tr, Kl, RA	04:00:00	07:00:00	4.8±0.2
2	2014-10-10	4	Ys, Kl, Ef, Tr, RA	20:30:00	00:30:00	12.2±0.8
3	2014-11-23	1	Ef, Tr, Kl, Sv, RA	05:00:00	06:00:00	20.2±0.8
4	2014-12-01	1	Ef, Sr, Kl, RA	21:00:00	22:00:00	51.3±0.8
5	2014-12-10	1	Sr, Tr, Sv, Zc, RA	10:00:00	11:00:00	28.4±0.8

* RA—space radio telescope RadioAstron (international project); Ef—Effelsberg (Germany), 100-m; Sr—Sardinia (Italy), 65-m; Kl—Kalyazin, Moscow Region (Russia), 64-m; Ys—Yebes (Spain), 40-m; Nt—Noto, Sicily (Italy), 32-m; Tr—Toruń (Poland), 32-m; Sv—Svetloye, Leningrad Region (Russia), 32-m; Sc—Zelenchuk, Karachay-Cherkess Republic (Russia), 32-m.

** Calibrated flux density of the strongest spectral feature at the velocity $V_{\text{LSR}} = -9.4$ km/s is given only for individual telescopes obtained from autospectra of individual telescopes—see explanation in the Discussion section.

about the velocity field on scales <1 AU around the central YSO. Note that in the RadioAstron project the water maser emission from the star-forming regions Orion KL and W49 N was detected on the projected ground-space baselines of ~ 3.5 and ~ 9.7 Earth diameters, respectively (for details, see. [22]).

2. OBSERVATIONS

We observed the H₂O masers of IC 1396 N in the period from July to December 2014 with the ground-space interferometer including the 10-m RadioAstron space telescope and a network of ground-based telescopes. RadioAstron was launched into orbit on July 18, 2011, from the Baikonur cosmodrome by a Zenit-3F rocket, using a Fregat-SB booster. This is the first ground-space radio interferometer operating in four radio bands from meter to centimeter wavelengths; it provides the highest angular resolution ever achieved of about $10 \mu\text{arcsec}$. The main interferometer parameters are described in [23] and presented in detail on the project website at <http://www.asc.rssi.ru/radioastron/index.html>.

The observations were performed at a frequency of 22.2280 GHz with a frequency resolution of ~ 7.81 kHz, i.e., a velocity resolution of 0.11 km/s, at the coordinates of the source $\text{RA}(2000) = 21^{\text{h}}40^{\text{m}}41.75^{\text{s}}$, $\text{DEC}(2000) = +58^{\circ}16'11.9''$. For the RadioAstron Space Telescope at a wavelength of 1.35 cm the System Equivalent Flux Density (SEFD) is 37 kJy [24].

IC 1396 N was observed in five sessions, that fall into three categories according to the size of the ground-space baselines: short baselines up to ~ 2.3 Earth diameters (July), medium baselines of ~ 3.8 ; Earth diameter (one session in October and one in December), and long baselines of ~ 5.9 and ~ 5.1 Earth diameters (in November and December, respectively). In Table 1 we list the average projected baseline lengths and angular resolutions for each of the five observing sessions. In Table 2 we list the date and time for each observing session, the participating radio telescopes and the peak flux density observed for the $V_{\text{LSR}} = -9.4$ km/s maser component.

Observations on the short baselines provide the highest probability of signal detection at ground-

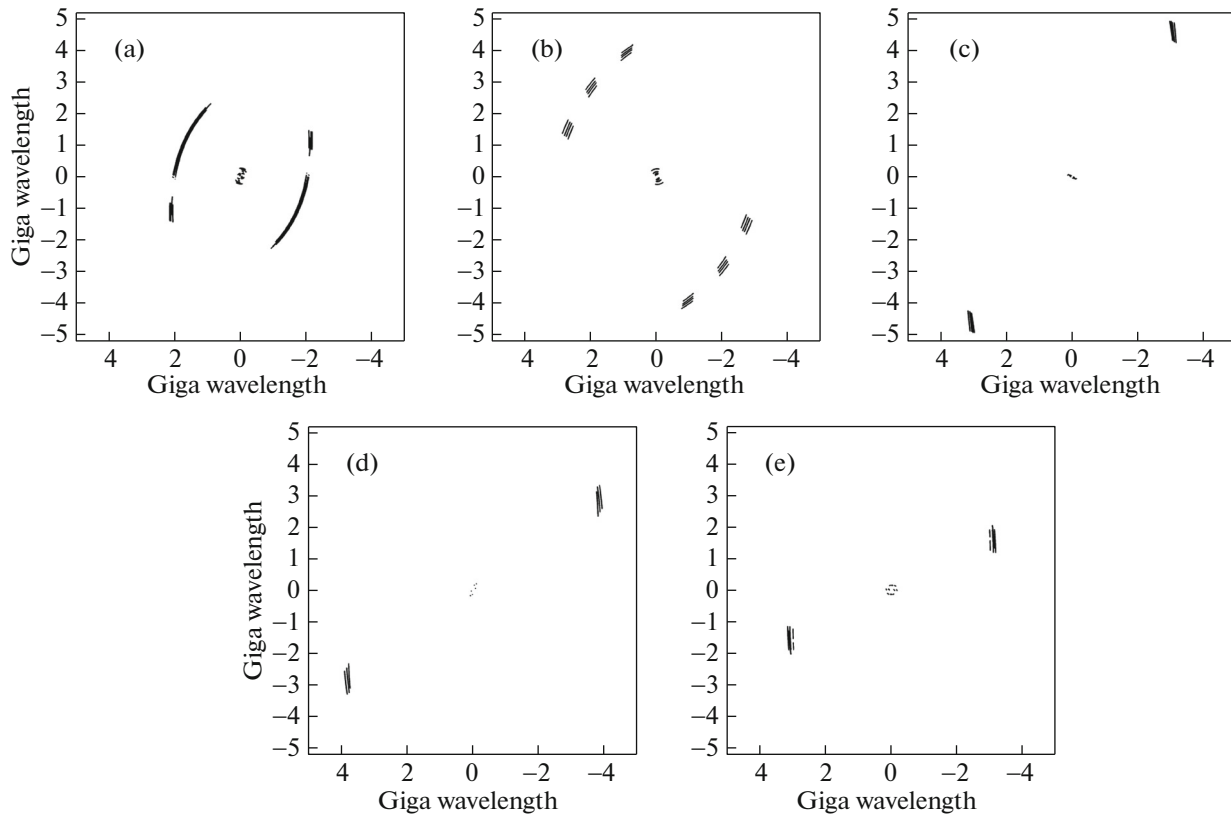


Fig. 1. The uv -plane coverage for the ground-space baselines of the 2014 observations (the data for all telescopes participating in the observations): (a) July, short baselines, session duration is 3 hours (session number 1 in Tables 1 and 2); (b) October, medium baselines, 4 hours (session number 2); (c) December, medium baselines, 1 hour (session number 3); (d) November, long baselines, 1 hour (session number 4); (e) December, long baselines, 1 hour (session number 5).

space baselines, and allow us to establish a lower limit on the maser size and an upper limit on the maser brightness temperature for unresolved source. The inclusion of medium baselines improves the spatial resolution and image quality compared to that obtained with only the short baselines. The longest baselines were included to permit the possible measurement of the maser spot size.

Plots of the ground-space uv coverage for each observing session are shown in Fig. 1 (the data shown are for all telescopes participating in the observations), in Fig. 2—we show the uv coverage of the ground-only baselines (the data shown are for only one baseline in each session, on which the signal was detected—the baselines shown are identified in Fig. 5).

3. DATA REDUCTION AND PRESENTATION OF THE RESULTS

Primary data processing was carried out with the software correlator at the Astro Space Center LPI [25]. The search for fringes on the ground-space baselines was performed using the software package PIMA (<http://astrogeo.org/pima/>).

Subsequent processing of FITS files was done with the AIPS software package (<http://www.aips.nrao.edu>). Amplitude calibration was performed with the task ANTAB, incorporating the antenna noise temperature measurements made at the time of the observations. Due to technical problems, recording of calibration tables at telescopes Ys, Sr and Nt (for a key to the telescope abbreviations, see Notes to Table 2) was not performed; in these cases we used standard values of the noise temperature calculated on the basis of known antenna parameters (http://www.evlbi.org/user_guide/EVNstatus.txt).

The quasar J2137+510 (RA(2000) = $21^{\text{h}}37^{\text{m}}01.0015^{\text{s}}$, DEC(2000) = $+51^{\circ}01'36.079''$) was used as the calibration source, and was observed for five minutes in each observing session at all ground telescopes. The primary calibration of the group delay signal and phase rate were performed with the task FRING, using J2137+510. Bandpass calibration was done using the same quasar. The absolute J2000 coordinates RA(2000) = $21^{\text{h}}40^{\text{m}}41.81^{\text{s}}$, DEC(2000) = $+58^{\circ}16'12.0''$ of the brightest spectral feature at $V_{\text{LSR}} = -9.4$ km/s (self-calibration was performed using this maser feature) were determined

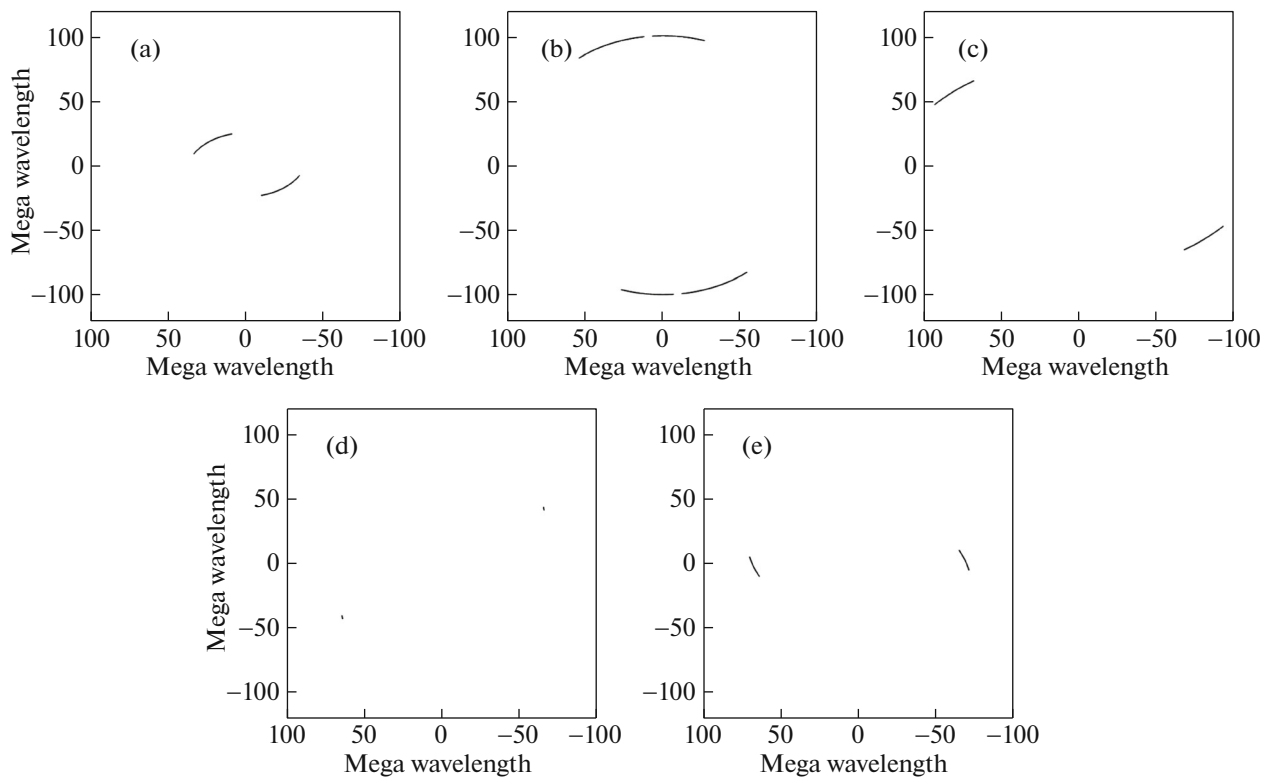


Fig. 2. Same as in Fig. 1, but for ground-ground baselines (data are shown for only one baseline in each session, on which the signal was detected—the corresponding baselines for each session are indicated in Fig. 5).

from fringe-rate mapping. Fringe rate (i.e. Doppler shift between signals received by antennas of an interferometer) is the function of the source coordinates and in the case of a single spectral line obtained on a single baseline is described by a straight line equation—crossing of several lines from different baselines indicates the position of the maser source on the map (method is discussed in detail in [26, 27]).

Figure 3 present uncalibrated (flux density in relative units) auto-correlation spectra for each session, i.e. spectra from each telescope participated in the observations. These spectra are used to diagnose the presence of the signal and to test the receiving equipment operability and the primary data quality. Figure 4 present the calibrated (flux density in Jy) auto-correlation spectra for the individual telescopes that were used to determine the flux density of the source for each session. Figure 5 present calibrated cross-correlation spectra (i.e. the result of multiplying of complex spectra received on individual telescopes) for only one baseline in each session on which the signal was detected. All spectra were constructed using the task POSSM, and the calibrated spectra were scaled using SETJY.

Positions and flux densities of maser spots relative to the reference spectral feature ($V_{\text{LSR}} = -9.4$ km/s) were determined by fringe rate mapping

(task FRMAP). All observing sessions had a reliable detection on the ground baselines of the two high-velocity maser features at $V_{\text{LSR}} = -9.4$ km/s and $V_{\text{LSR}} = +4.4$ km/s. For the low-velocity features, only the second epoch (October) resulted in detections at the 4σ level or higher.

In Fig. 6 we present fringe rate maps for the low-velocity features observed in the October 2014 session, covering multiple components from about -4.6 to $+1$ km/s. These features roughly separate into four groups consisting of maser spots nearby to one another on the sky—see Table 3 for their coordinates and the Discussion section for a description of the four groups. The figure illustrates the convergence of the solutions obtained by the fringe rate analysis. In Table 3 for the central part of the spectrum (displayed as an example in Fig. 7 in channels and velocities for second observation session) we list the derived positional offset on a channel-by-channel basis for those channels that had emission above a 4σ level.

4. RESULTS OF THE ANALYSIS

Fringes from IC 1396 N on the ground-space baselines were not detected in any of the observing sessions. This could have two causes: either the Radio Astron sensitivity was insufficient or the source is

Table 3. Maser component parameters derived from fringe-rate maps analysis for each channel from the central part of H₂O spectrum of IC 1396 N observed in the second session of 2014 observations (duration 4 hours)*

Spectral feature number	Maser group number	Channel number	V_{LSR} , km/s	ΔRA , mas	ΔDec , mas	Flux density, Jy
1	1	115	0.7	75.9 ± 1.5	-59.1 ± 2.1	0.3
2		116	0.6	85.6 ± 2.2	-50.8 ± 2.9	0.5
3		117	0.5	74.9 ± 1.4	-59.2 ± 2.0	0.7
4		118	0.3	79.0 ± 0.6	-49.6 ± 0.9	0.8
5		119	0.2	76.7 ± 0.3	-58.8 ± 0.4	0.7
6		120	0.1	87.4 ± 1.2	-55.9 ± 1.8	0.6
7		121	0.0	84.1 ± 1.0	-61.6 ± 1.6	0.5
8		122	-0.1	81.6 ± 0.5	-49.4 ± 0.9	0.5
9		123	-0.2	82.9 ± 0.8	-50.7 ± 1.2	0.5
10		124	-0.3	81.0 ± 0.4	-57.9 ± 0.6	0.4
11	2	133	-1.2	163.1 ± 1.3	-23.5 ± 1.8	0.5
12		134	-1.3	163.0 ± 0.2	-14.6 ± 0.3	0.5
13		135	-1.4	166.1 ± 0.3	-14.8 ± 0.5	0.6
14		136	-1.5	170.6 ± 1.4	-13.8 ± 1.8	0.7
15		137	-1.7	170.0 ± 1.0	-17.5 ± 1.4	0.6
16		138	-1.8	173.2 ± 0.4	-11.3 ± 0.5	0.5
17		139	-1.9	175.6 ± 0.5	-13.2 ± 0.7	0.4
18	3	142	-2.1	297.5 ± 1.2	79.3 ± 1.6	0.3
19		143	-2.3	293.2 ± 0.8	85.4 ± 1.2	0.4
20		144	-2.4	292.8 ± 0.3	77.8 ± 0.3	0.5
21		145	-2.5	288.4 ± 1.3	76.5 ± 1.9	0.4
22	4	150	-3.0	72.8 ± 0.5	-52.6 ± 0.6	0.4
23		151	-3.1	73.0 ± 1.3	-55.6 ± 1.4	0.5
24		152	-3.2	74.7 ± 1.1	-54.6 ± 1.4	0.6
25		153	-3.3	79.4 ± 0.7	-43.5 ± 0.8	0.5
26		154	-3.4	71.8 ± 0.4	-59.1 ± 0.5	0.5
27		155	-3.6	75.9 ± 0.5	-53.5 ± 0.7	0.4
28		156	-3.7	83.2 ± 1.3	-48.1 ± 1.6	0.4
29		163	-4.4	84.1 ± 0.8	-43.8 ± 0.9	0.3
30		164	-4.5	75.9 ± 5.3	-56.1 ± 7.6	0.3

* The reference high-velocity feature ($\Delta\text{RA} = 0$, $\Delta\text{Dec} = 0$) is at $V_{\text{LSR}} = -9.4$ km/s, flux density 5.5 Jy. The position of the second high-velocity feature at $V_{\text{LSR}} = +4.4$ km/s with flux density 1.7 Jy is $\Delta\text{RA} = 153.2$, $\Delta\text{Dec} = 146.3$.

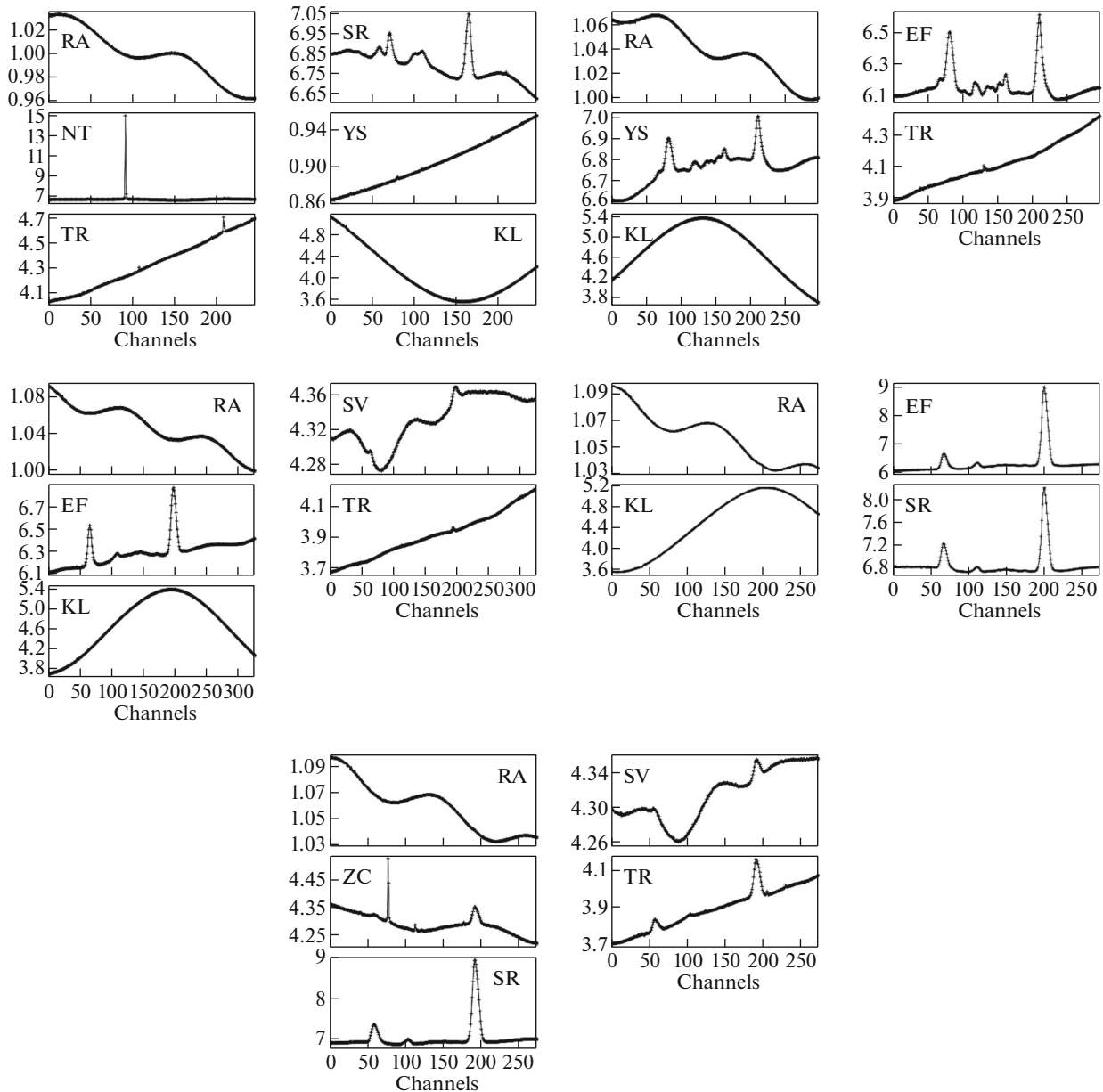


Fig. 3. Initial uncalibrated auto-correlation spectra for all telescopes participating in the 5 observing sessions. For a key to the telescope abbreviations, see Notes to Table 2.

larger than can be detected with such high resolution. We explore these two options below.

First, we consider the flux calibration of the data, and the resulting measured values for the maser flux densities. The Effelsberg 100-m telescope (Ef) participated in three observing sessions (the second, third, and fourth). Moreover, for this telescope we have ANTAB tables that contain information on antenna temperatures and antenna gain curves; thus an accurate flux calibration is possible for these three sessions. In the first session, the Sardinia 65-m radio telescope (Sr) was the only telescope with a detection. It lacked an ANTAB table, so the default SEFD

was used. In the fifth session, several telescopes detected emission, with Sardinia being the largest of these. Nevertheless, we based the calibration on the spectrum of the Toruń 32-m telescope (Tr), because it had an ANTAB table, so its flux density could be determined more reliably than by using the default SEFD of the Sardinia telescope.

In Table 2 the flux density of the strongest spectral feature at the velocity of -9.4 km/s, derived from the auto-correlation spectra (see Fig. 4) is presented for each session. These values were determined using the ORIGIN package (<http://www.originlab>).

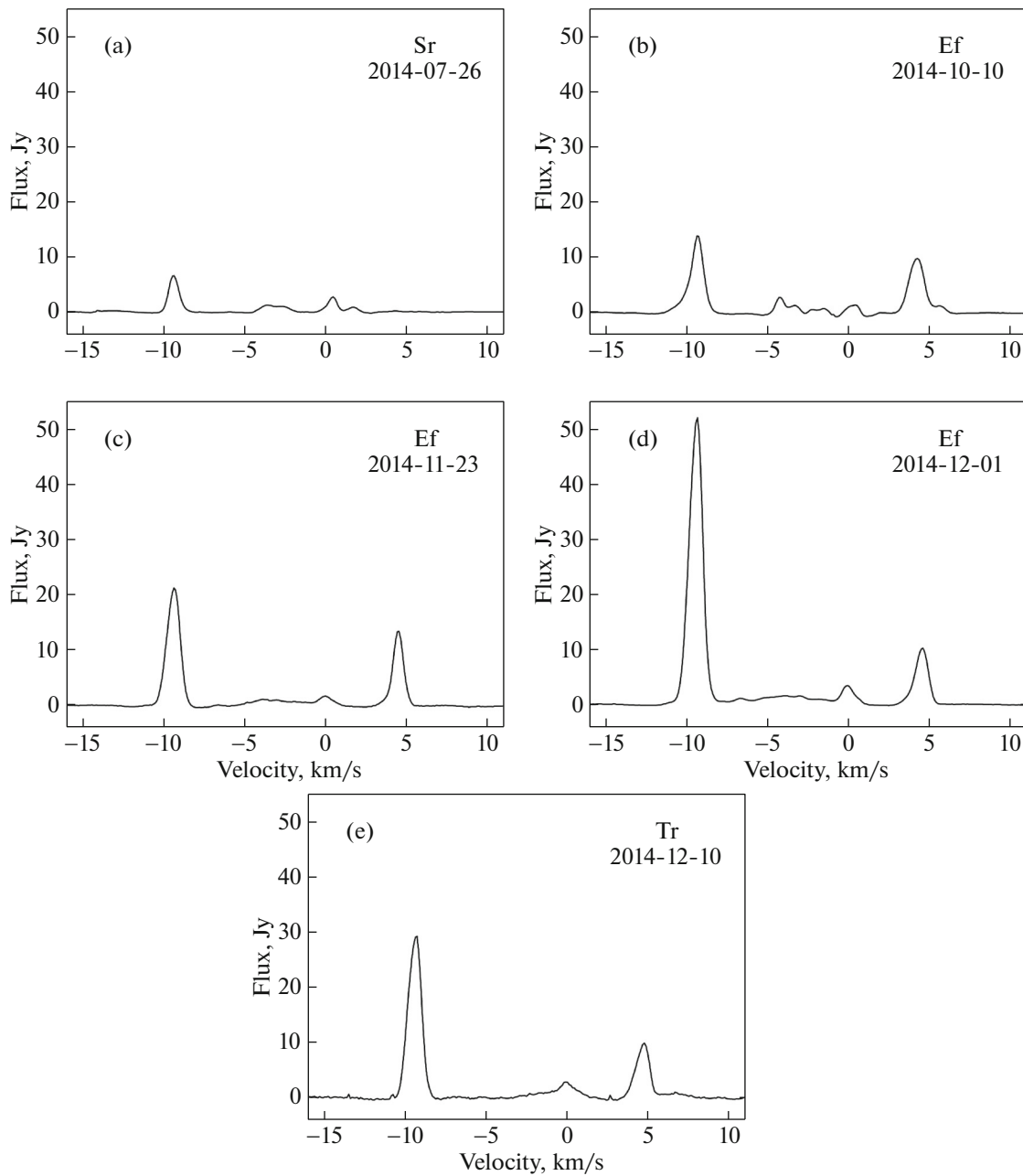


Fig. 4. Calibrated auto-correlation spectra for individual telescopes that were used to determine the source flux density in each session of the observations. The telescope and the date are indicated in the upper right corner.

com/) by a procedure of the Fit Gaussian program task.

From the auto-correlation spectra (Fig. 4) strong source variability is evident. The strongest flux density of ~ 51 Jy was during the fourth observing session (Fig. 4d); the weakest flux density (~ 5 Jy) was in the first session (Fig. 4a).

If we adopt the 5 Jy flux density as a lower limit, then the lack of correlations with the space-telescope indicates that the source brightness temperature at the time of the observations was lower than $6.25 \times$

10^{12} K. The lack of correlation on the shortest baseline of 2.3 ED means that the linear source size is $L > 0.03$ AU.

In each session of the observations maser emission was detected on a single ground-ground baseline, as indicated in Fig. 5. The telescopes not involved in the detection were flagged before further processing with FRMAP. In these detections, H_2O maser emission at the 4σ level is present over a range of velocities from about -10 km/s to $+5$ km/s. There is no high-velocity blue feature at $V_{\text{LSR}} = -14.1$ km/s [16], or

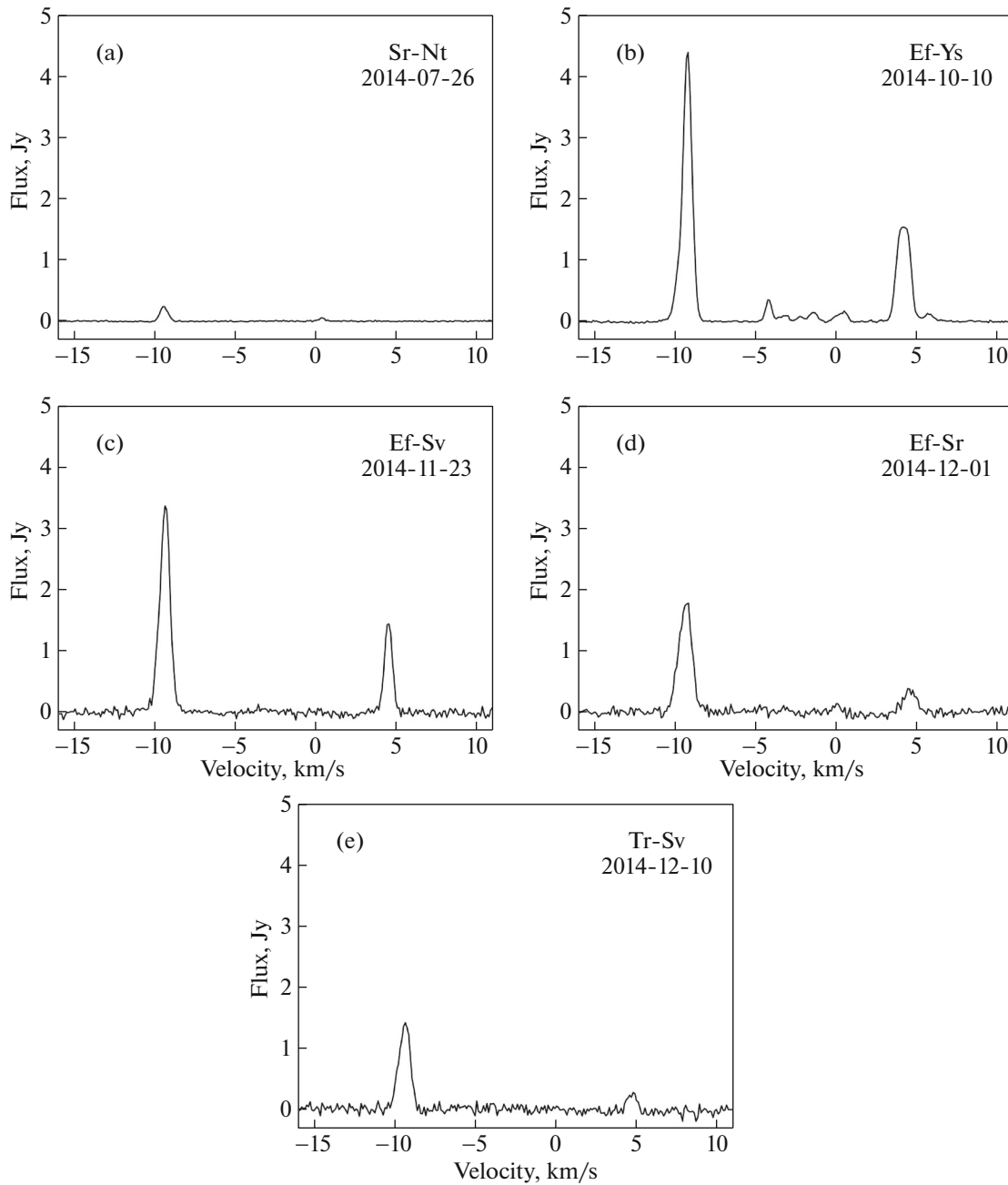


Fig. 5. Calibrated cross-correlation spectra (Stokes I) for only one baseline (indicated in the upper right corner) in each session for which the signal was detected.

at $V_{\text{LSR}} = -14.6$ km/s [17]. Nor is there a high-velocity red feature at $V_{\text{LSR}} = +9.3$ km/s, as observed by [16]. Rather, there are two new and bright features: a blue one at $V_{\text{LSR}} = -9.4$ km/s and a red one at $V_{\text{LSR}} = +4.4$ km/s.

The central, low-velocity part of the spectrum is much fainter than in the observations reported by [16], but it covers a broader range from $V_{\text{LSR}} = -4.5$ km/s to $V_{\text{LSR}} = +0.7$ km/s. The feature at $+1.32$ km/s,

used for the self-calibration in [16], is not present in our spectra.

5. DISCUSSION

5.1. Analysis of the Maps and Position-Velocity Diagrams

Figure 8 presents a map of the H₂O maser spots for the central part of the spectrum in the velocity range -4.5 km/s to $+0.7$ km/s and also of the two

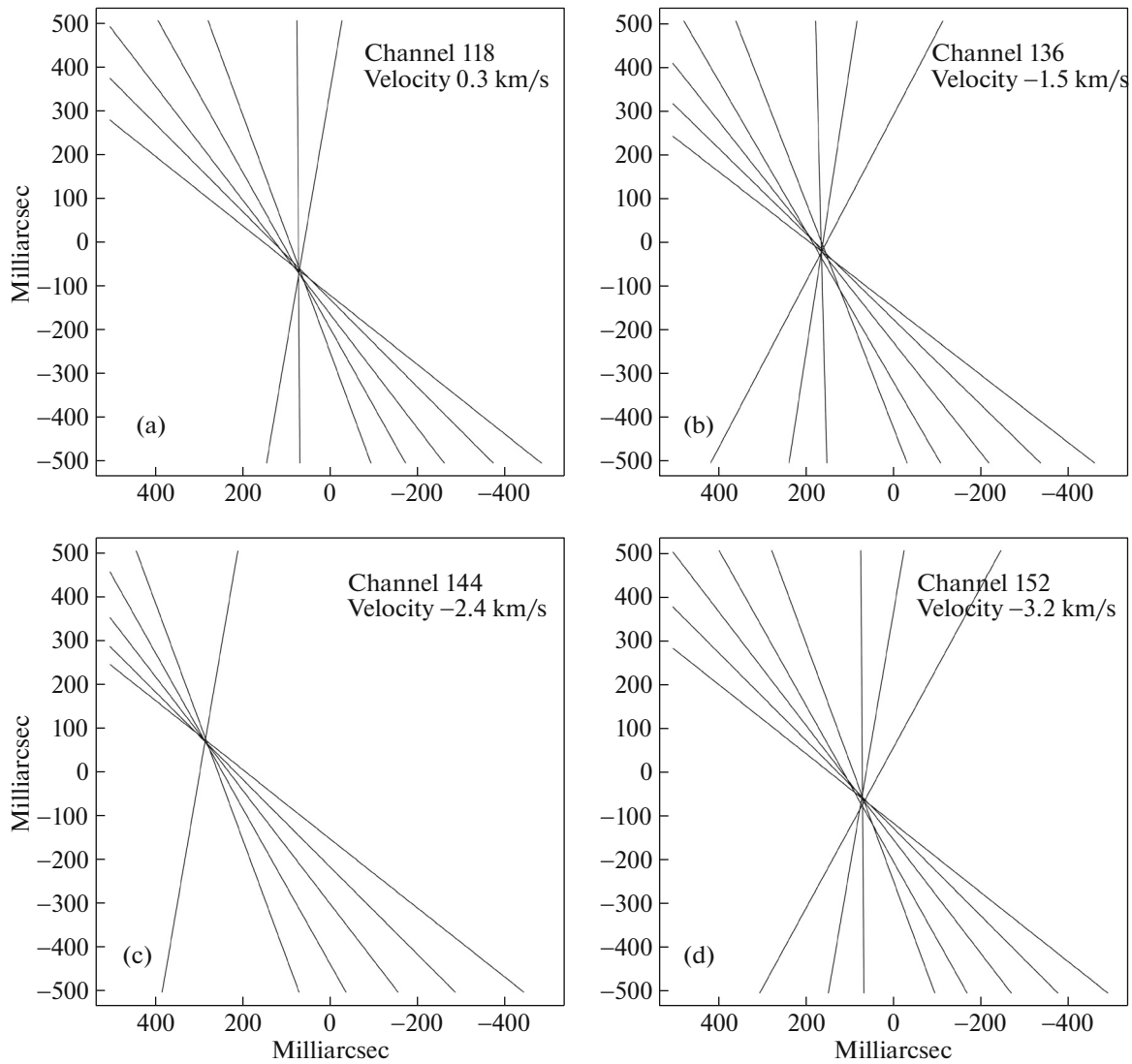


Fig. 6. Maps determined by fringe rate mapping (task FRMAP) for the brightest spectral features in each of the four low-velocity groups observed in the second epoch; see Table 3 and the description of the velocity groups in the Discussion section. The channel number and the corresponding velocity are given in the upper right corner of each panel.

high-velocity features at $V_{\text{LSR}} = -9.4$ km/s and at $V_{\text{LSR}} = +4.4$ km/s. The fitted maser positions in each velocity channel are listed in Table 3. The map was produced from data taken during the second observing session. The maps are in Dec–RA offset coordinates, given relative to the strongest maser feature at the velocity $V_{\text{LSR}} = -9.4$ km/s (Fig. 8a); on Fig. 8b positions are given relative to maser feature at the velocity $V_{\text{LSR}} = +0.3$ km/s (see explanations below).

The maser components given in Table 3 are divided into 4 groups, according to their velocities. The 1st and 4th groups are very close to one another on the sky (see Fig. 8); i.e., *dynamically* there are four groups, but *spatially* there are only three groups. The central spatial cluster has a spread less than

about 20 mas and includes the 1st and 4th maser groups with velocities in the -4.5 to $+0.7$ km/s range. Two other spatial clusters—the 2nd and 3rd maser groups—also with spreads each ~ 20 mas, have velocities in the -2.5 to -1.2 km/s range. Two high-velocity masers are isolated in position and are found at projected distances of 157 AU and 70 AU, respectively, from the central spatial cluster. These three maser clusters fall in a straight line, about 200 AU in length, as shown in Fig. 8.

In the analysis of [17] the reference feature for all maser spots was the high-velocity blue component at $V_{\text{LSR}} = -14.6$ km/s. This component was detected by [16] (albeit with a velocity difference of ~ 0.5 km/s), but was not used as their reference maser. Rather, their reference component was at

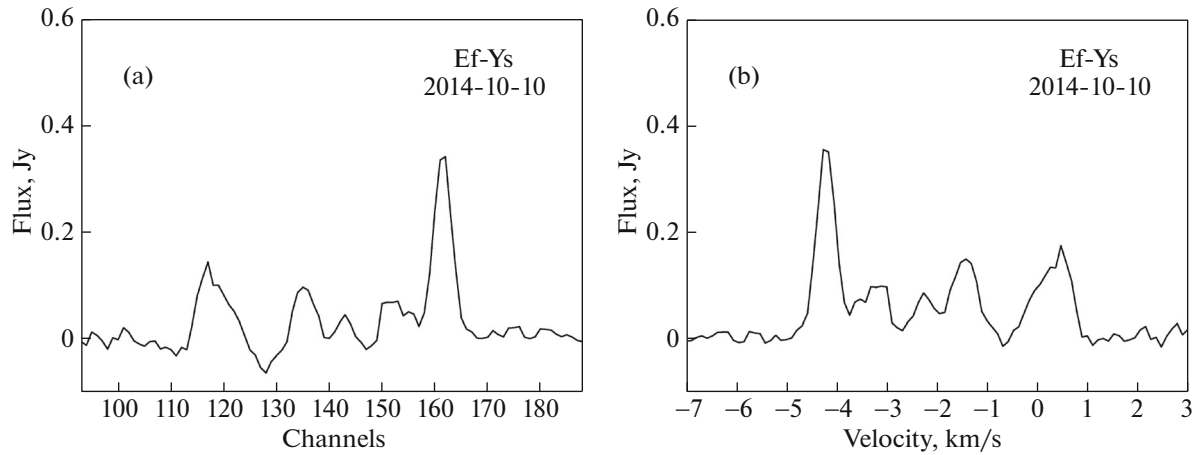


Fig. 7. The central part of the cross-correlation spectra for the second session of the observations. On the Y axis is the calibrated flux density; on the X axis at the left (a) are channels, at the right (b) is line-of-sight velocity.

$V_{\text{LSR}} = +1.32$ km/s in the central range of the spectrum. [16] report the relative coordinates of the $V_{\text{LSR}} = -14.1$ km/s component, which permits us to recalculate the coordinates of this feature in the reference frame of [16] and hence to compare the two observations. This recalculation shows that the differences in the velocities and in the absolute coordinates of this component between the two surveys does not exceed the uncertainties from both observations: the features observed in [16] coincide with the group “B” in [17]. According to the conclusions of [16], 8 maser spots of this group form a disk of size 15 AU, while according to [17] the masers in the central part “L” of this group form a loop with a radius of ≤ 1 AU; they suggest that the loop is associated with a circumstellar shell of outflowing stellar-wind material.

The same conversion can be made for the coordinates of the spectral feature from the reference maser at $V_{\text{LSR}} = -9.4$ km/s, re-scaling to the frame of the feature at $V_{\text{LSR}} = +0.3$ km/s in our observations (see Fig. 8b). This velocity feature is the only one common to all three spectra: ours, and those of [17] and [16]. By this coordinate conversion we can compare all three data sets and hence arrive at more robust conclusions. Although the other features (besides the feature at $V_{\text{LSR}} = +0.3$ km/s) detected in 1996 by [16, 17] were not present at the 2014 epoch, we include these masers in our analysis.

In Fig. 9 we show the maser positions of all three epochs (this paper, [16, 17]), calculated relative to the velocity feature at +0.3 km/s. Included in Fig. 9 are the masers from the central part of the spectrum and also the high-velocity components. The positions from our observations correspond to the second session of 2014 and are shown as blue circles (numbers on the map correspond to maser groups

from Table 3). The features from [17], are from the central and the more distant “A position” (letters in Fig. 9 correspond to maser groups from [17]) at the velocity $V_{\text{LSR}} = -14.6$ km/s, and are shown as green circles. Finally, the masers from [16], including the high-velocity feature at $V_{\text{LSR}} = -14.1$ km/s but not the most distant red feature at $V_{\text{LSR}} = +9.3$ km/s, are shown as red circles.

In Fig. 10a relative to the velocity +0.3 km/s the Velocity-Right Ascension diagram ($V_{\text{LSR}}\text{-RA}$) is shown for the same session for the central part and two distant spots $V_{\text{LSR}} = -9.4$ km/s and $V_{\text{LSR}} = +4.4$ km/s. Two linear structures are evident in Fig. 10a: one consisting of the features with velocities more positive than $V_{\text{LSR}} = +0.3$ km/s (the first, second, and third groups; see Table 3), and a second linear structure consisting of the two high-velocity components and the fourth maser group centered at velocity $V_{\text{LSR}} = -3.4$ km/s.

In the combined distribution in Fig. 9 and 10b the same linear structures are seen. Also evident is the loop structure observed in 1996 [17] and the putative Keplerian disk, also observed in 1996 [16], which corresponds to group one, as observed in 2014 (see Table 3). In other words, over an 18-year period, the spatial structure of the maser spots in the central part of the IC 1396 N globule are confined to the velocity interval ± 1.5 km/s around $V_{\text{LSR}} = +0.3$ km/s, on a scale less than 20 mas or 15 AU at a distance of 750 pc.

5.2. Possible Models of the Source

Slysh et al. [16] considered a combined model of a Keplerian disk surrounding a YSO along with a stellar wind from the central object; indeed, it is possible that

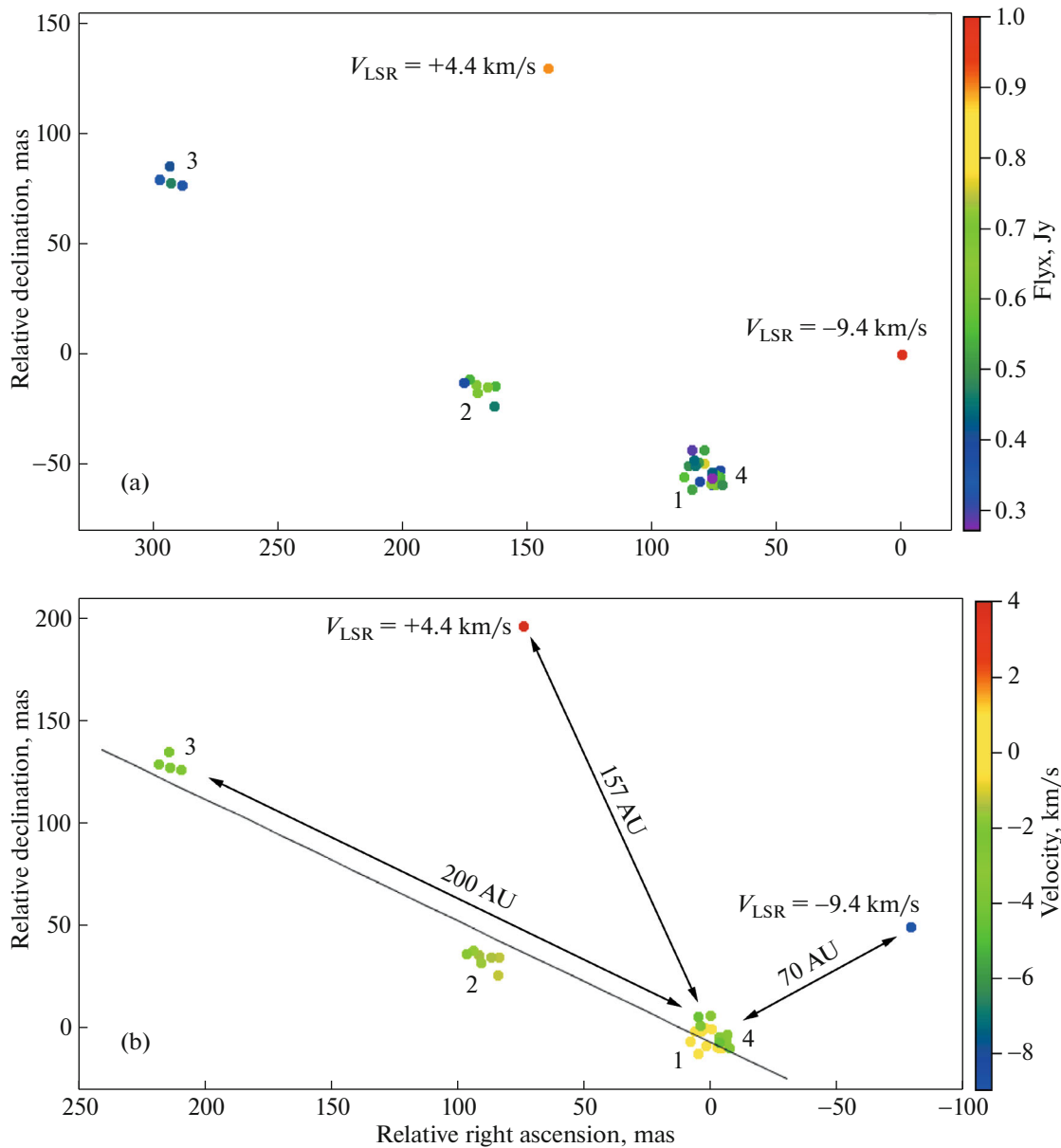


Fig. 8. Maps of the H₂O maser components in IC 1396 N in relative Dec–RA coordinates for the second session of 2014 observations. The central range of the spectrum (maser groups 1–4) and two high-velocity components are presented. At Fig. 8a coordinates are given relative to the reference high-velocity blue feature at the velocity $V_{\text{LSR}} = -9.4$ km/s (a color scale of the flux density), at Fig. 8b coordinates are re-scaled to the frame of the feature at $V_{\text{LSR}} = +0.3$ km/s (a color scale of the velocity).

different mechanisms may be simultaneously involved in the formation of the observed pattern.

Groups 2 and 3, are spatially separated from the central (groups 1, 4) cluster and were first detected only in 2014. They might be caused by a high-velocity jet from the central object/cluster. As seen from the map (Fig. 8b), groups 2 and 3 are located almost along a straight line with respect to the central cluster at a distance of 200 AU. The putative jet in Fig. 8 is collimated to a narrow opening angle not exceeding

5° . These distant features were not detected in [17]; see the combined map in Fig. 9.

In [17] there are two features that we did not detect in 2014. These are shown as green circles in Fig. 9—one labeled as C (hv1996) and the other as D (hv1996). These masers may correspond to the two high-velocity components that we mention in the footnote of Table 3. The presence of high-velocity masers suggests the action of a collimated outflow from the vicinity of the central object. The increase of velocity along the line connecting these

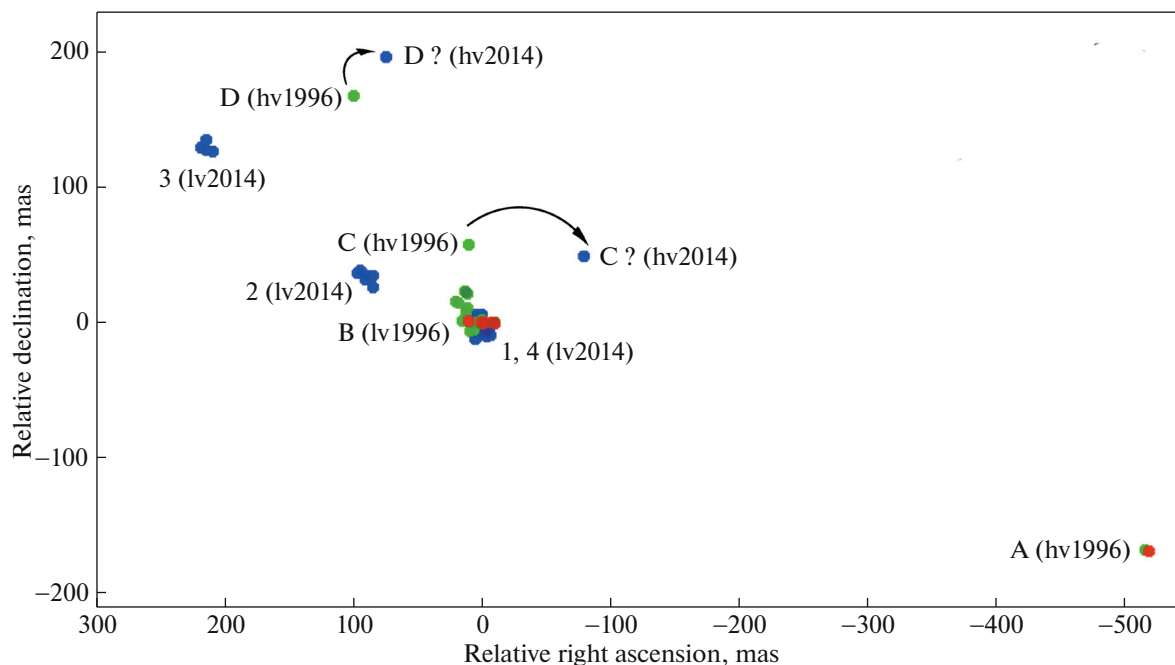


Fig. 9. Combined map of the H₂O maser spots in IC 1396 N obtained in 2014—the blue circles and numbers on the map correspond to maser groups from Table 3; 1996—the green circles and letters correspond to maser groups from [17]; and also 1996—red circles from [16] (without the distant red feature at velocity $V_{LSR} = +9.3$ km/s, which is incompatible with the scale of the map). High-velocity components from the observations of 2014 are indicated with “hv2014”, from [17] are indicated by “hv1996”. Similarly, we denote the low-velocity components: 2014—“lv2014”, [17]—“lv1996”. Coordinates were recalculated with the +0.3 km/s feature as the reference position.

details could arise from the progressive acceleration of the flow by, say, a stellar wind from the central object. It can be assumed that in the 18 years since the 1996 observations of [17] (green circles C(hv1996) and D(hv1996) in Fig. 9) and our observations (blue circles C?(hv2014) and D?(hv2014) in Fig. 9), the direction of the outflow has changed by about 30° (see calculations below); this is illustrated by the curved arrows in Fig. 9.

The outflow velocity carrying maser features to a distance of nearly 200 AU in 18 years must be fairly high—about 56 km/s. This velocity is sufficient to ionize ambient hydrogen gas and to produce free-free radio continuum. There are some centimeter and millimeter continuum studies of IRAS 21931+5802, e.g., at BIMA by [3]. However, their angular resolution [3] (a few arcseconds) is not high enough to definitely associate the observed radio structures with the above-mentioned putative jet exciting the maser features. A higher resolution radio continuum study of the jet region would be valuable.

A variety of mechanisms have been proposed to explain the collimation of outflows from young stellar objects (e.g., [28–31]): (1) collimation near the stellar surface related to infalling circumstellar material; (2) collimation by a circumstellar structure (a disk or torus); (3) self-focusing of the stellar wind in the

surrounding interstellar medium; and (4) magnetohydrodynamic mechanisms in the vicinity of the star. In the case of IC 1396 N, no data on the stellar magnetic field are available, so nothing can be said about the effect of mechanism (4). In particular, no emission from the magneto-sensitive hydroxyl molecule has been detected.

In view of the evidence for a circumstellar disk in IC 1396 N, we focus here on mechanism (2). An interesting phenomenon is the change in direction of the putative outflow with time.

A possible cause is the precession of a protoplanetary disk by the influence of the secondary component of a binary system. Such a case is discussed in detail, for example, in [32], who report an expression for the angular velocity of the disk precession. Applying their expression, however, yields precession periods of several thousand years for stellar masses of a few solar masses and a semi-major orbital axis of a few astronomical units.

It seems more likely that the collimation and the precession of the outflow are driven by a larger circumstellar structure—a torus inside the globule [18–20], see Fig. 11. This torus is clearly visible in molecular emission (e.g., N₂H⁺ and CH₃CN [2]) as a structure perpendicular to the direction of the

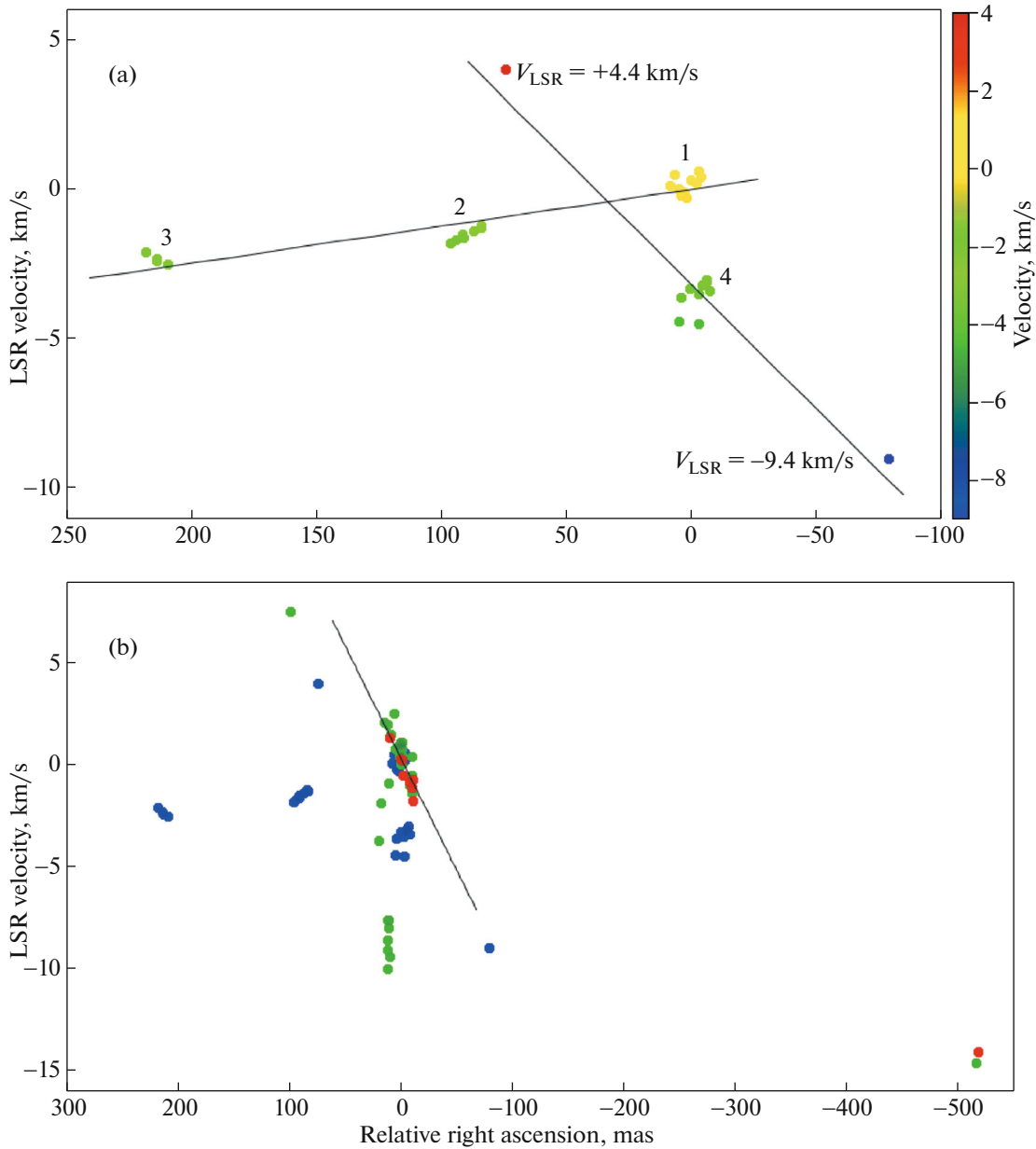


Fig. 10. Right ascension—velocity diagram (V_{LSR} -RA) for the maser components of Fig. 8 (corresponds to 10a) and Fig. 9 (corresponds to 10b). See description in the text.

bipolar outflow. Molecular line data for the circumstellar structure around IRAS 21391+5802 [33] yield a virial mass in the range of 83–186 M_{\odot} . Molecular data indicate that the density in clumps is decreasing outward as $\rho \propto r^{-\alpha}$, where $\alpha \sim 1$, see [20] and references therein. Adopting for the circumstellar torus a mass of 134 M_{\odot} and sizes of 0.06–0.14 pc ($\sim 2\text{--}4 \times 10^{17}$ cm) [33], imply that the inner cavity radius (see Fig. 11) is $R_1 = H = 3 \times 10^{15}$ cm, while the “effective” outer radius (with $\alpha = 1$) is $R_2 = 3 \times 10^{16}$ cm. We then find from the formula in [18] a disk precession period $T_{\text{pr}} \sim 160$ years. Thus, in the

18 years between Patel et al.’s and our observations the disk could have precessed by about one tenth of 360° , in fair agreement with the $\sim 30^\circ$ we see in Fig. 9.

5.3. Is IC 1396 N Losing Its Protoplanetary Disk?

Another peculiarity of IC 1396 N is a continuous decline of its H_2O maser emission seen in our Pushchino monitoring during the last 10 years [34]. Throughout the first half of the 2000–2010 period the maximum H_2O line flux density F_{max} in IC 1396 N was maintained at a level of hundreds of janskys. On December 19, 2014, the closest date to epoch

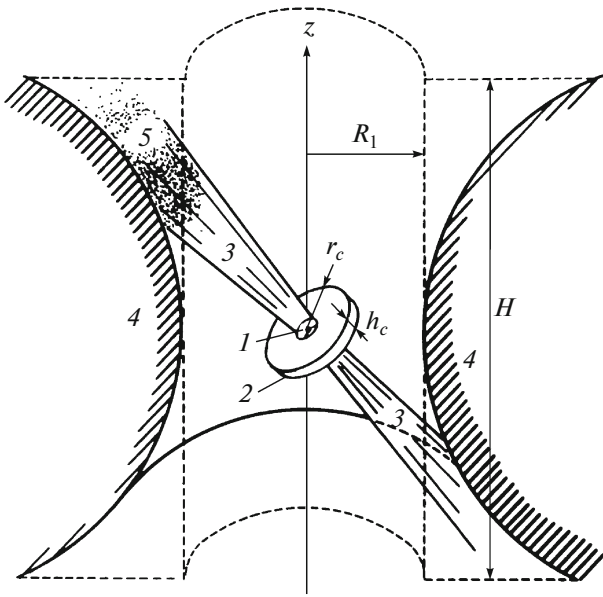


Fig. 11. Sketch of the model of the source with a precessing disk [18]; 1—star, 2—protoplanetary disk, 3—jets, 4—circumstellar torus, 5—bright maser spot.

No. 5 of our RadioAstron observations, it was about 50 Jy; by June 2016 it fell to 20 Jy, and it is continuing to decrease at the time of submission of this paper. If the observed trend persists, this may imply the disappearance of the protoplanetary disk in IC 1396N, which hosted the main features of H₂O maser emission. Such a rapid evolution of the circumstellar structure in IC 1396 N seems plausible. Rapid changes on a timescale of a few years were observed in the infrared spectrum of the young solar-like star TYC 8241 2652 1. From 2008 to 2012 the flux of its emission between 3 and 300 μm decreased by a factor of about 30 [35]. This decrease is interpreted by the loss of the dust component of the circumstellar protoplanetary disk because of its concentration into larger bodies (planetesimals). Thus, the formation of planets in circumstellar disks may be much more rapid than previously thought. Perhaps we have managed to catch IC 1396 N just at the stage when a drastic restructuring of the protoplanetary disk results in the decay of H₂O maser emission. A follow-up monitoring program of the H₂O maser in IC 1396 N would confirm or reject this hypothesis.

6. CONCLUSIONS

(1) During observations of H₂O masers in the IC 1396 N globule using the ground-space interferometer with the 10-m space radio telescope RadioAstron, no response from the source was detected on projected baselines >2.3 ED. A lower limit on the size of the masers is $L > 0.03$ AU; an upper limit on the brightness temperature is $T_B = 6.25 \times 10^{12}$ K.

(2) An analysis of the maps obtained by fringe rate mapping for the session with the longest observing time (4 hours) on the ground baselines was performed. Parameters of maser spots—positions, velocities, and flux densities—were determined for those maser features with $\text{SNR} > 4\sigma$.

(3) Maser groups at low velocities (in the interval from -4.5 km/s to $+0.7$ km/s) were detected, as were two high-velocity features at $V_{\text{LSR}} = -9.4$ km/s and $V_{\text{LSR}} = +4.4$ km/s. The latter two are spatially offset from the strongest feature at ~ 0.3 km/s at distances of 157 AU and 70 AU, respectively.

(4) Maser components of the central part of the spectrum can be divided into four groups based on their velocities. However, two groups (the first, with a V_{LSR} of about $+0.3$ km/s, and the fourth, with a V_{LSR} of about -3.4 km/s) spatially coincide.

(5) On the (RA–Dec) maps, four groups of central components form a chain of maser spots, which is nearly a straight line of about ~ 200 AU in extent. Two groups—the second (~ -1.5 km/s) and the third (~ -2.4 km/s)—were not detected in 1996 and perhaps trace a jet that formed during the 18 year period between 1996 and 2014.

(6) The appearance of the high-velocity features “C” and “D” in 2014 at the different from 1996 [17] spatial coordinates might be explained by the precession of the collimated outflow under the influence of gravity from the YSO.

(7) There is a straight line orientation (V_{LSR} –distance) seen in the (V_{LSR} –Right Ascension) diagram between the jet and the first low-velocity group at $V_{\text{LSR}} \sim +0.3$ km/s, whereas the high-velocity components are aligned with the 4th group at $V_{\text{LSR}} \sim -3.4$.

(8) The (V_{LSR} –Right Ascension) diagram shows that the low-velocity maser spots of 1996 and 2014 maintain their positions near the central velocity $V_{\text{LSR}} \sim +0.3$ km/s during the 18 year period.

(9) The observed continuous decline of the H₂O maser emission in IC 1396 N, especially conspicuous from 2014 to 2016, may indicate a drastic restructuring of the circumstellar protoplanetary disk due to the rapid formation of planets within it.

ACKNOWLEDGMENTS

The RadioAstron project is led by the Astro Space Center of the Lebedev Physical Institute of the Russian Academy of Sciences and the Lavochkin Scientific and Production Association under a contract with the Russian Federal Space Agency, in collaboration with partner organizations in Russia and other countries.

Partly based on observations with: the 100-m telescope of the MPIfR (Max-Planck-Institute for Radio Astronomy) at Effelsberg; the Sardinia and Noto Radio Telescopes operated by INAF—Istituto di Radioastronomia; RT-40 telescope in Yebes Observatory operated by IGN—The National Geographic Institute of Spain; the Toruń 32-m telescope of the Centre for Astronomy Nicolaus Copernicus University and radio telescopes of IAA RAS (Federal State Budget Scientific Organization Institute of Applied Astronomy of Russian Academy of Sciences). We are grateful to the astronomy observatories for the opportunity to observe with the radio telescopes and to the staff of the observatories for their assistance in carrying out the observations.

This work was partially supported by the Russian Foundation for Basic Research—project 15-02-07676-a (GMR), project 16-32-00877-mol_a (OSB) and UNAM/DGAPA (project IN114514) (SEK). We thank Dr. S.V. Kalenskii for assistance in drafting the observing proposal.

REFERENCES

1. H. E. Matthews, *Astron. Astrophys.* **75**, 345 (1979).
2. A. Fuente, T. Castro-Carrizo, T. Alonso-Albi, M. T. Beltrán, C. Ceccarelli, B. Lefloch, C. Codella, and P. Caselli, *Astron. Astrophys.* **507**, 1475 (2009).
3. M. T. Beltrán, J. M. Girart, R. Estalella, P. T. P. Ho, and A. Palau, *Astrophys. J.* **573**, 246 (2002).
4. C. Codella, R. Bachiller, B. Nisini, P. Saraceno, and L. Testi, *Astron. Astrophys.* **376**, 271 (2001).
5. K. Sugitani, Y. Fukui, A. Mizuni, and N. Ohashi, *Astrophys. J.* **342**, L87 (1989).
6. B. A. Wilking, R. D. Schwartz, L. G. Mundy, and A. S. B. Schultz, *Astron. J.* **99**, 344 (1990).
7. A. L. Gyulbudaghian, L. F. Rodríguez, and S. Curiel, *Rev. Mex. Astron. Astrofis.* **20**, 51 (1990).
8. K. A. Edris, G. A. Fuller, and R. J. Cohen, *Astron. Astrophys.* **465**, 865 (2007).
9. V. I. Slysh, I. E. Val'tts, S. V. Kalenskii, M. A. Voronkov, F. Palagi, G. Tofani, and M. Catarzi, *Astron. Astrophys. Suppl. Ser.* **134**, 115 (1999).
10. S. V. Kalenskii, R. Bachiller, I. I. Berulis, I. E. Val'tts, J. Gomez-Gonzalez, J. Martin-Pintado, A. Rodriguez-Franco, and V. I. Slysh, *Sov. Astron.* **36**, 517 (1992).
11. R. Simon, J. M. Jackson, J. M. Rathborne, and E. T. Chambers, *Astrophys. J.* **639**, 227 (2006).
12. N. Peretto and G. A. Fuller, *Astron. Astrophys.* **505**, 405 (2009).
13. C. J. Cyganowski, B. A. Whitney, E. Holden, E. Braden, C. L. Brogan, E. Churchwell, R. Indebetouw, D. F. Watson, B. L. Babler, R. Benjamin, M. Gomez, M. R. Meade, M. S. Povich, T. P. Robitaille, and C. Watson, *Astron. J.* **136**, 2391 (2008).
14. G. Tofani, M. Felli, G. B. Taylor, and T. R. Hunter, *Astron. Astrophys. Suppl. Ser.* **112**, 299 (1995).
15. V. Migenes, S. Horiuchi, V. I. Slysh, I. E. Val'tts, V. Golubev, P. G. Edwards, E. B. Fomalont, R. Okayasu, P. J. Diamond, T. Umemoto, and M. Inoue, *Astrophys. J. Suppl. Ser.* **123**, 487 (1999).
16. V. Slysh, I. Val'tts, V. Migenes, E. Fomalont, H. Hirabayashi, M. Inoue, and T. Umemoto, *Astrophys. J.* **526**, 236 (1999).
17. N. A. Patel, L. J. Greenhill, J. Herrnstein, Q. Zhang, J. M. Moran, P. T. P. Ho, and P. F. Goldsmith, *Astrophys. J.* **538**, 268 (2000).
18. G. M. Rudnitskij, in *Star Forming Regions, Proceedings of the IAU Symposium No. 115, Tokyo, Japan, Nov. 11–15, 1985*, Ed. by M. Peimbert and J. Jugaku (D. Reidel, Dordrecht, 1987), p. 398.
19. G. M. Rudnitskij, *Bull. Astron. Inst. Czechosl.* **69**, 51 (1987).
20. I. I. Berulis, E. E. Lekht, and G. M. Rudnitskij, *Astron. Rep.* **40**, 36 (1996).
21. J. F. Lightfoot, *Mon. Not. R. Astron. Soc.* **239**, 665 (1989).
22. N. S. Kardashev, A. V. Alakoz, A. S. Andrianov, M. I. Artyukhov, et al., *Vestn. NPO im. S.A. Lavochkina* **3**, 4 (2016).
23. N. S. Kardashev, V. V. Khartov, V. V. Abramov, V. Yu. Avdeev, et al., *Astron. Rep.* **57**, 153 (2013).
24. u. A. Kovalev, V. I. Vasil'kov, M. V. Popov, V. A. Soglasnov, P. A. Voitsik, M. M. Lisakov, A. M. Kut'kin, N. Ya. Nikolaev, N. A. Nizhel'skii, G. V. Zhekanis, and P. G. Tsybulev, *Cosm. Res.* **52**, 393 (2014).
25. A. S. Andrianov, I. A. Girin, V. E. Zharov, V. I. Kostenko, S. F. Likhachev, M. V. Shatskaya, *Vestn. NPO im. S. A. Lavochkina* **3**, 55 (2014).
26. R. C. Walker, *Astron. J.* **86**, 1323 (1981).
27. L. Kogan, in *Astronomical Data Analysis Software and Systems V*, Ed. by G. H. Jacoby and J. Barnes, *ASP Conf. Ser.* **101** (1996).
28. R. Bachiller, *Ann. Rev. Astron. Astrophys.* **34**, 111 (1996).
29. L. F. Rodríguez, *Publ. Astron. Soc. Pacif.* **98**, 1012 (1986).
30. L. F. Rodríguez, in *Proceedings of Star Formation 1999, Nagoya, Japan, June 21–25, 1999*, Ed. T. Nakamoto (Nagoya Univ., Nagoya, 1999), p. 257.
31. D. J. Price, T. S. Tricco, and M. R. Bate, *Mon. Not. R. Astron. Soc.* **423**, L45 (2012).
32. D. Lai, *Mon. Not. R. Astron. Soc.* **440**, 3532 (2014).
33. J. Wu, N. J. Evans II, Y. L. Shirley, and C. Knez, *Astrophys. J. Suppl. Ser.* **188**, 313 (2010).
34. N. Ashimbaeva, O. Bayandina, P. Colom, E. Lekht, M. Pashchenko, G. Rudnitskij, A. Tolmachev, and I. Val'tts, Talk Presented at Symposium No. 9, European Week of Astronomy and Space Science, Athens, Greece, July 4–8, 2016.
35. C. Melis, B. Zuckerman, J. H. Rhee, I. Song, S. J. Murphy, and M. S. Bessell, *Nature* **487**, 74 (2012).